AIAA JOURNAL
Vol. 62, No. 5, May 2024

Investigation of Burst Pressure of Flat-Scored Metal Diaphragms in Hypersonic Impulse Facilities

Wentao Wang,* Qiu Wang,† Jinping Li,‡ and Wei Zhao§
Chinese Academy of Sciences, 100190 Beijing, People's Republic of China
and
Liangjie Gao,¶ Zhongchen Liu,¶ and Zhansen Qian**
AVIC Aerodynamics Research Institute, 110034 Shenyang, People's Republic of China

https://doi.org/10.2514/1.J063581

Flat-scored metal diaphragms are essentially used in various hypersonic impulse facilities as quick-opening valves. Their burst pressure is a key parameter to optimize the performance of shock wave experimental devices and ensure the activation of overpressure safety devices. However, the conventional method to predict the burst pressure relies on time-consuming experiments that pose significant challenges for ultrahigh driving conditions. In this study, the finite element method (FEM) based on the Johnson–Cook model is adopted to predict the burst pressure of diaphragms used in a shock tube. The influences of the diaphragm thickness and groove depth on the burst pressure are analyzed. A simplified approximation based on the simulation results is obtained to estimate the burst pressure under a static load rapidly. This method is more generalizable than the existing equation and produces results in good agreement with experimental results. Furthermore, the burst pressure is investigated under different dynamic loads using the proposed FEM method. The results show that the dynamic load results in larger burst pressures than the static load, indicating that the burst pressure depends on the load type, the loading rate, and the magnitude of the applied forces.

Nomenclature

A, B, C, m, n	=	Johnson–Cook strength model constants, MPa
a, b, c	=	coefficients of burst pressure
C_p	=	isobaric specific heat, J/(kg · K)
D	=	damage state variable
D_1, D_2, D_3, D_4, D_5	=	Johnson–Cook damage model constants
d	=	diameter of diaphragm, mm
E	=	Young's modulus, GPa
K	=	thermal expansion, 1/K
N	=	grid number across grooves
p	=	pressure, MPa
R	=	open variable
T	=	material temperature, K
t	=	diaphragm thickness, mm
α	=	thermal conductivity, W/(m · K)
β	=	Taylor–Quinney coefficient
ΔT	=	adiabatic temperature rise, K
ε	=	groove depth, mm
ε_p	=	equivalent plastic strain
$\dot{\varepsilon}$	=	strain rate, s^{-1}
$\varepsilon_{\text{pl}}^f$	=	failure strain
η	=	stress triaxiality
μ	=	Poisson's ratio
ρ	=	material density, kg/m^3
σ	=	material flow stress, MPa
τ	=	current load time, ms
τ_0	=	total load duration, ms

Subscripts

m	=	melting value
r	=	reference value
s	=	static load

Superscript

$*$	=	nondimensionalization by reference value

I. Introduction

FLAT-SCORED metal diaphragms have been used successfully in various hypersonic shock tubes/tunnels and gas guns. These diaphragms function as quick-opening valves that separate the driving and driven sections and are essential for ensuring undisturbed flow by opening instantaneously. Numerous studies have investigated diaphragm rupture issues, such as the time and distance for shock formation [1–5], nonideal diaphragm ruptures, and the influence on the shock wave evolution [4–10]. This paper focuses on predicting the diaphragm burst pressure, which is essential for designing efficient test conditions and safe operations to maintain the burst pressure within reasonable limits before each shot. This fundamental role of the diaphragm is critical for combustion or detonation-driven facilities that use flammable gases. Therefore, the diaphragm must operate correctly to prevent a hang fire.

Diaphragms are usually flat metal disks in hypersonic impulse facilities, and they are grooved to adjust the burst pressure and minimize fragmentation. Predicting the burst pressure of diaphragms typically relies on extensive experiments to establish empirical or semi-empirical relationships between the pressure and relevant diaphragm parameters. However, this approach is inefficient, especially when testing different diaphragm materials or structures. Most published experimental results were obtained with light-gas guns.

Received 17 September 2023; revision received 18 December 2023; accepted for publication 25 December 2023; published online 19 January 2024.

*Ph.D. Student, State Key Laboratory of High-Temperature Gas Dynamics, Institute of Mechanics; also School of Engineering Science, University of Chinese Academy of Sciences, 100049 Beijing, People's Republic of China.
†Associate Professor, State Key Laboratory of High-Temperature Gas Dynamics, Institute of Mechanics; wangqiu@imech.ac.cn (Corresponding Author).
‡Associate Professor, State Key Laboratory of High-Temperature Gas Dynamics, Institute of Mechanics.
§Professor, State Key Laboratory of High-Temperature Gas Dynamics, Institute of Mechanics; also School of Engineering Science, University of Chinese Academy of Sciences, 100049 Beijing, People's Republic of China.
¶Associate Professor, Aeronautical Science and Technology Key Lab for High Speed and High Reynolds Number Aerodynamic Force Research.
**Professor, Aeronautical Science and Technology Key Lab for High Speed and High Reynolds Number Aerodynamic Force Research.

The existing semi-empirical equation describing this single driving mode has an open variable whose value must be derived from experiments or simulations [11]. Additionally, conducting experiments with ultrahigh driving pressures poses significant challenges. For instance, light-gas gun [12] or free-piston shock tunnel [13] experiments in which the diaphragm burst pressure can reach up to 50 MPa are nearly impossible to perform due to the capacity limitations of the pressure-loading equipment or safety considerations.

However, it is now possible to perform numerical simulations of the response of structures to loads involving transient or long durations, large material deformation, and material damage and failure. The results can provide detailed information on the rupture dynamics of the diaphragm, and this approach is more efficient and less costly than experiments. Tretjakovas et al. [14] conducted simulations of the rupture of diaphragms with different defect depths and found that deeper grooves moderated the stress concentration at the clamped location of diaphragms. Colombo et al. [15] revealed that increasing the diaphragm thickness exacerbated the instability during crack propagation, resulting in a more asymmetrical deformation during the diaphragm opening. Although some researchers have considered factors influencing the burst pressure [16,17], they only conducted qualitative analyses. Only a few studies, such as those by Rast [18] and Helminiak [19], used quantitative analyses of the effective/total thickness. Quantitative numerical simulations of flat-scored diaphragms have not been conducted systematically, although they are a simple method for predicting the burst pressure, as demonstrated by Colombo et al. [15]. Additionally, the reviewed studies primarily focused on diaphragms subjected to quasi-static loads. It should be noted that the effective driving pressure in experiments may require some time to reach the peak, which may be longer than the rupture process. As Prickett's experiments [20] showed, the bearing capacity of metal sheets increased under high loading rates, highlighting the importance of the dynamic material characteristics. Several studies [16,21,22] have demonstrated the similarity of deformation between the diaphragms and the disks. However, the diaphragm burst pressure under dynamic loads has been rarely studied. Therefore, there is a lack of comprehensive analyses of the burst pressure of diaphragms in impulse facilities, necessitating further in-depth investigations.

In view of the importance of the prediction of the diaphragm burst pressure for the operation of hypersonic impulse facilities, such as shock tubes and shock tunnels, the primary goal of this study is to estimate the burst pressure for different diaphragm structures and load profiles. The finite element method (FEM) with a detailed numerical model is applied. The burst pressure of diaphragms with different thicknesses, groove depths, and widths is examined. A simplified approximation is obtained to estimate the burst pressure under a static load quickly and accurately. The burst pressures under step and dynamic loads are discussed to investigate the mechanisms for guiding diaphragm design in hypersonic impulse facilities.

II. Model and Numerical Method

A. Diaphragm Specification

This paper focuses on diaphragm issues at a particular facility, namely, JFX, a shock tunnel located in the State Key Laboratory of High-Temperature Gas Dynamics (LHD), Institute of Mechanics, Chinese Academy of Sciences (CAS). The facility consists of a driving section and a driven section with lengths of 6.6 and 6.9 m, respectively, and the same inner diameter of 126 mm. A curved opening with a radius of 8 mm in the driven section next to the diaphragm is considered in the geometric model. Figure 1 shows the diaphragm details relevant to the rupture process. The dumping section, nozzle, and test section were not considered in this study. More information on the shock tunnel can be found in Ref. [23].

The diaphragm material depends on the operational characteristics of the shock tube, such as the pressure, temperature, and gas composition in the driving tube. The material includes simple polymer films, such as cellophane [24] and Mylar [25], and common metals, such as brass, aluminum, and stainless steel [26–28]. However, a flat-scored metal diaphragm is generally used in impulse facilities with high-pressure operating conditions, such as in the JFX shock tunnel. It has

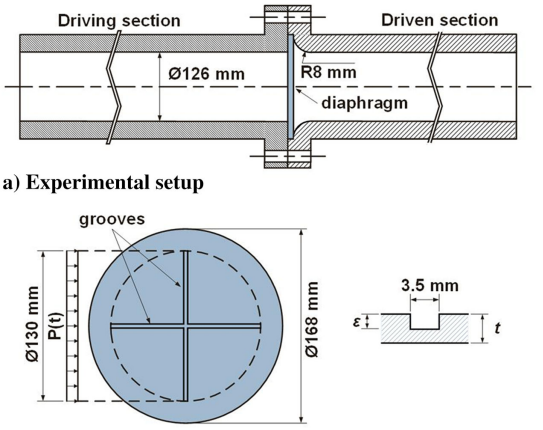

Fig. 1 Schematic view of diaphragm in the JFX shock tunnel.

a maximum pressure exceeding 20 MPa and a maximum temperature of 3000 K in the driving section, where a hydrogen–oxygen mixture is ignited [29]. X-shaped scored steel diaphragms with different thicknesses and groove depths are used to adjust the critical bursting pressure and minimize fragmentation. When the predetermined bursting pressure has been reached, the diaphragm ruptures and tears along the grooves, forming petals that fold back against the tube wall, not hindering the gas flow. The two grooves of the diaphragm have 90° angles, and the groove cross section is rectangular, as shown in Fig. 1. The length and width of the scored grooves are 130 and 3.5 mm, respectively, and are the same in all simulations. The diaphragm's notched side faces the driven section, and the diaphragm is clamped by two flanges and tightened by 12 bolts.

The plates are made of stainless steel 304, which has high elongation and relatively high ultimate strength in the annealed condition. Stainless steel plates can withstand a high degree of deformation without fragmenting. The material is assumed to be homogeneous and isotropic in this study. The diaphragms have the same geometry and are made of the same material as those typically used in shock tube tests. The cause of diaphragm rupturing in this study is overpressure, rather than other causes such as defects, line perforations from piercers, or cuts from knife edges. Thus, the important factors affecting rupturing are the diaphragm thickness t and the groove depth ε (the dimensionless ratio ε/t is used in this study and is referred to as the depth hereafter).

Experimental tests were conducted to obtain the burst pressure at the failure of the scored diaphragms with different thicknesses and groove depths and validate the simulation results. The driving section was pressurized by a high-pressure tank (∼10 MPa). The pressure in the driven section was maintained below 10 kPa using an air pump. The air entry into the chamber was controlled by an electrovalve connected to a remote PC that stops pumping after the diaphragm has ruptured. The resulting pressure variation was linear, with an average loading rate of 0.0022 MPa/s. The pressure evolution inside the pressurized chamber was monitored by pressure transducers. This method is universal and applicable to other facilities, although the diaphragm parameters are based on the JFX shock tunnel.

B. Numerical Modeling

The deformation and rupture characteristics of the diaphragm are analyzed using the finite element (FE) software Abaqus. The focus is on the burst pressure of the diaphragm before the rupture, without considering the opening process when the driving gas expands into the driven tube. Thus, the issue is simplified by directly applying the load profiles in the FE model. Since a large pressure difference exists between the driven (∼kPa) and driving (∼MPa) sections, the force exerted by the test gas is ignored, and only the pressure of the driving gas is considered. The diaphragms are loaded by a uniform pressure maintained over a circular inner area, whose diameter corresponds to the internal pressurized chamber size (126 mm). The loaded area is

shown in Fig. 1. The translational and rotational degrees of freedom of the outer annulus of the diaphragm that contacts the tube are zero.

The diaphragm has double-axial in-plane symmetry. Therefore, only a quarter of the system with a symmetric boundary is considered the three-dimensional FE domain. Figure 2 shows the one-quarter section view of the 3D FE model, retaining part of the low-pressure section tube that is 80 mm long. The low-pressure section tube serves as a circumferential constraint and is modeled as a rigid body without considering tube vibration or elastoplastic deformation.

1. *Load Profiles*

The load exerted on a diaphragm is influenced by the behavior of the high-pressure driving gas on the upstream side. In the JFX and similar shock tube/shock tunnel setups, a predetermined quantity of a hydrogen–oxygen mixture is typically introduced into the high-pressure section before the operation. It is essential for efficient and safe operation to maintain the burst pressure within close limits in order to achieve the ignition of the flammable mixture before the diaphragm bursts and prevent a premature explosion. This scenario is required in all shock tube and shock tunnel configurations because the diaphragm must withstand the initial inflation pressure before each shot. Once a shot begins, the gas in the driving section is ignited or compressed to generate sufficiently high pressure, causing the diaphragm to burst and the formation of an incident shock. Generally, shock tube flow simulations use the driving gas overpressure as the initial condition. It should be noted that the pressure rise requires a certain amount of time that depends on the driving mode.

The variations in the load profiles, such as the duration, pressure peak, and growth rate, can significantly influence the response of a structure. Two types of loading conditions are considered in the present simulations: static and dynamic loads. The static load is required to determine the burst pressure in impulse facilities. Experimental tests to obtain this burst pressure are regarded as quasi-static processes, in which the gas pumping time is much longer than the structural response time of the diaphragm. Rather than an explicit pressure–time curve, a total pressure value is assigned in the simulations and divided into small increments. Nonlinear static equilibrium equations are then used to derive the strain after each increment until it reaches the critical value. This strategy enables us to obtain the failing pressure of the diaphragm, which corresponds to the static burst pressure.

The dynamic load represents the dynamic pressure applied to the diaphragm. Figure 3 shows three typical pressure profiles. The abscissa is normalized by the total recorded time, while the ordinate is normalized by the average peak pressure. The recorded times for normalization are 3, 90, and 35 ms for the detonation, free-piston, and combustion curves, respectively, which correspond to the peak pressures of 31.35, 45.37, and 6 MPa. The detonation curve (red) is obtained using data from a pressure transducer located in front of the diaphragm of the JFX shock tunnel [29]. An ignition tube is generally used to induce the detonation. However, the three-dimensional structure of the ignition tube can cause reflection and diffraction of the detonation wave. This complex flow causes pressure oscillations

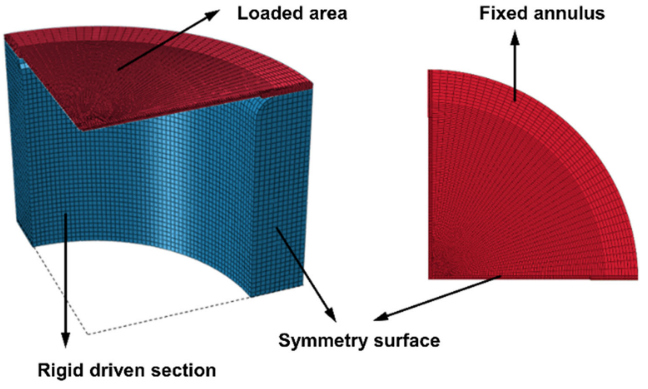

Fig. 2 One-quarter-section view of the 3D FE model, boundary conditions, and mesh distribution.

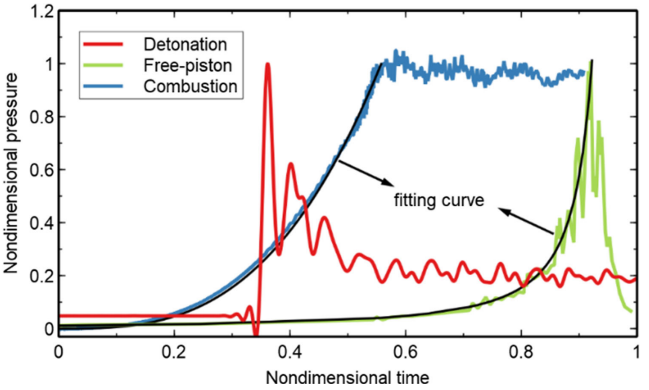

Fig. 3 Typical nondimensional pressure–time curves for dynamic loads.

close to the diaphragm, but they attenuate with distance [30]. The free-piston load curve generally uses pressure data near the secondary diaphragm, such as that in the light gas gun DBR30 [12] or the expansion tube X3 [24]. The piston is propelled by impulse loads from the reflected wave initiated by the detonation or the compressor. Under this action, the diaphragm is in a fluctuating pressure environment due to pressure waves rebounding throughout the driving tube as the piston rapidly compresses the gas. The combustion load curve is obtained from shock tube tests by igniting a hydrogen–air mixture in the driving section on the tube axis [31]. The pressure exhibits a smooth increase as the cylindrical flame surface extends radially and decays slightly as the high-temperature gas dissipates heat into the wall after complete combustion. The two black curves represent functional approximations to the pressure histories of the free-piston and combustion driving modes, respectively. The two fitted profiles are applied to the same diaphragm with different peak pressures and loading durations. A detailed discussion of this approach is provided in Sec. III.

2. *Material Model*

The large deformation behavior of the diaphragm material for different strain rates requires an appropriate method to capture the characteristics of the large deformation and rupture processes under quasi-static and dynamic loads, especially for the latter. The strengthening effects of the strain, the strain rate, and the softening effect of the temperature should be considered. The complex damage and failure process of the material cannot be adequately described by a physically based constitutive equation; therefore, phenomenological relationships are often used in simulations [32]. The Johnson–Cook (JC) model is widely utilized to describe the stress–strain behavior for different strain rates and temperatures because it is suitable for computational procedures. This study uses the JC plasticity model [33] to model the flow stresses of an isotropic material. This dynamic criterion model performs nonlinear fitting of the strain, strain rate, and temperature:

$$\sigma = \sigma(\varepsilon, \dot{\varepsilon}, T) = (A + B\varepsilon_p^n)(1 + C\ln(\dot{\varepsilon}_p^*))(1 - (T^*)^m) \quad (1)$$

where σ is the flow stress, ε_p is the equivalent plastic strain, $\dot{\varepsilon}_p^* = \dot{\varepsilon}/\dot{\varepsilon}_0$ is the dimensionless strain rate, $\dot{\varepsilon}_0$ is the reference strain rate (which is typically 1 s^{-1}), and T^* is the homologous temperature defined as $T^* = (T - T_r)/(T_m - T_r)$, where T_r is the reference temperature and T_m is the melting temperature of the material. The material constants are A, B, n, C, and m. The JC model parameters under dynamic loads for stainless steel 304 are obtained from [34]. This set of JC parameters is suitable for a high strain rate, but it can only describe the material behavior correctly when the strain is less than 0.3 at a quasi-static strain rate of 0.001 s^{-1}. Therefore, the static JC parameters obtained from [35] are modified to ensure that the reference strain rate is 1 s^{-1} in the stress–strain curve before the damage occurs.

Ductile and shear failure of the material may occur under high-strain-rate deformation. The former is attributed to the nucleation,

growth, and coalescence of voids, whereas the latter is caused by the formation of shear band localization [36]. Both criteria use the equivalent plastic strain as the failure criterion, which is achieved by integrating the strain rate components over time. The JC damage model [33] is employed as the ductile failure criterion:

$$\varepsilon_f^p = (D_1 + D_2 e^{-D_3\eta})(1 + D_4 \ln(\dot{\varepsilon}_p^*))(1 + D_5 T^*) \tag{2}$$

where ε_f^p is the current failure strain, η is the stress triaxiality defined as the ratio of the pressure stress to the Von Mises stress, ε_p^* is the dimensionless strain rate, and T^* is the homologous temperature, the same as in Eq. (1). $D_1 - D_5$ are material constants. After the plastic deformation occurs, the damage accumulates, and the stress increases as the equivalent strain increases monotonically until the tensile strength is reached; then, the stress decreases. The stress degradation follows the relationship $\sigma_D = \sigma(1 - D)$, where $D = \sum(\Delta\varepsilon_p/\varepsilon_f^p)$ is the damage parameter. It is considered that the material fails until the state variable D reaches a value of 1. The element is then removed from the FEM model by Abaqus.

In addition, some driving modes, such as detonation and combustion, occur under high-temperature operating conditions. However, the heat transfer from the hot gas to the diaphragm is negligible during a short period because the total time for diaphragm opening is in the order of milliseconds. Meanwhile, it is acceptable to assume that this process is adiabatic. Most of the plastic strain energy of metallic materials is dissipated into heat, resulting in a temperature rise [37]. Therefore, the flow stress is calculated and incorporated into the JC strength model using the following relationship:

$$\Delta T = \frac{\beta}{\rho C_p} \int \sigma \mathrm{d}\varepsilon_p \tag{3}$$

where ρ is the material density, C_p is the isobaric specific heat, and β is the Taylor–Quinney coefficient, representing the percentage of plastic work converted to heat; the value is typically 0.9. The parameters of the stainless steel 304 are listed in Table 1. It is worth noting that the damage constants under a static load are not given because the pressure remains constant for a relatively long time in the quasi-static experiment. Once the maximum stress of the diaphragm reaches the tensile strength, the pressure pushes the material to the failure point. Thus, the criterion for the diaphragm rupture under a static load is the maximum strain value of 0.638.

3. *Grid Independence Study*

The mesh density is crucial in this study because the criteria for diaphragm rupture are based on material failure. Defining the diaphragm rupture is an important step in this research because it has not been explicitly addressed in other investigations. Before rupturing, the diaphragm bulges due to the increasing pressure of the gas, forming a dome. The strain energy accumulated during the deformation. When the strain energy density of an element exceeds the failure criteria, the element is removed, resulting in a hole, indicating the occurrence of rupture. Both simulations and experiments indicate that the diaphragm failure typically occurs at the corner of the groove intersection due to the stress concentration, as shown in Fig. 4. In the simulations, the diaphragm rupture is defined as the occurrence of holes at the corner of the groove intersection. In the experiments, it is characterized by a sudden increase in the gage value in the driven section.

A grid convergence study was conducted on the diaphragm with a thickness of $t = 1.8$ mm and a groove depth of $\varepsilon = 1.4$ mm. The mesh was generated by scaling the global mesh size proportionally. The main focus of the grid setup was the grooves. An equally spaced mesh was applied, where the mesh size was $1/N$ of the groove width. Thus, there were N grids in the groove width direction, and N ranged from 10 to 200. Figure 5 shows the burst pressure for different grid resolutions. It is evident that the simulated burst pressure decreases quickly with mesh refinement in the early stage. This result can be attributed to the fact that a lower mesh density requires a higher energy supply for an element to rupture. After the burst pressure reaches its maximum, it converges gradually to a constant that is the mesh-independent value. In the present case, a mesh size of 1/100 of the groove width is used, and acceptable convergence is obtained.

Table 1 Material properties of stainless steel 304

Parameter	Static/dynamic value
ρ	8000
E	207.8
μ	0.3
A, B, n, C, m	260, 1150, 0.68, 0, 1/280, 802.5, 0.622, 0.0799, 1
$D1$, $D2$, $D3$, $D4$, $D5$	—/0.69, 0, 0, 0.0546, 0
$\dot{\varepsilon}_0$	1
T_m	1673
T_r	1000
K	17.8E−6
α	16.2
β	0.9
C_p	452

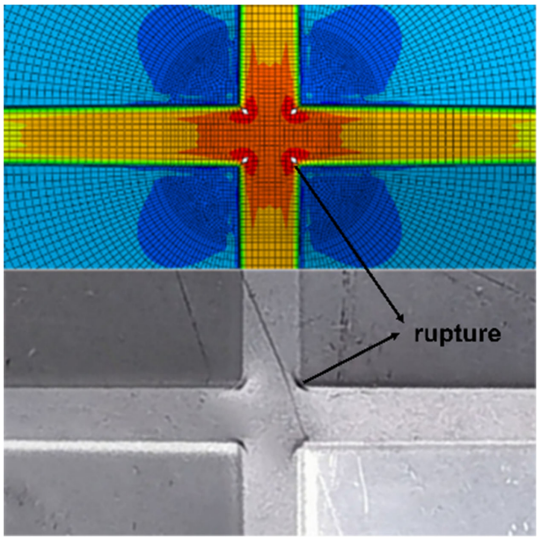

Fig. 4 Rupture characteristics of the diaphragm in the simulations (top, $N = 20$ as an example) and quasi-static loading experiments (bottom).

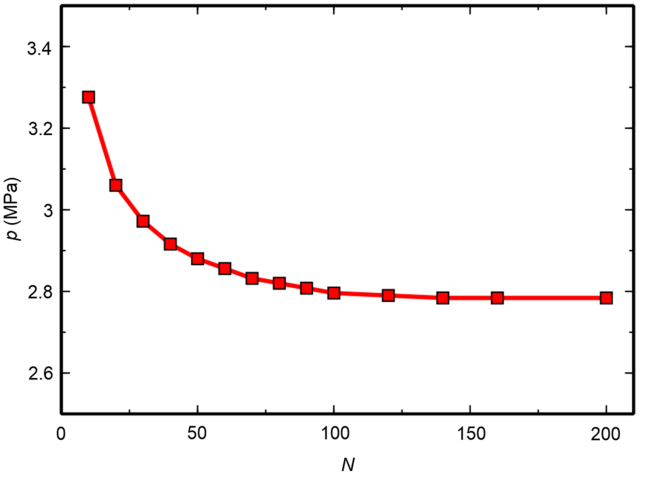

Fig. 5 Predicted burst pressure obtained from mesh sizes with $t = 1.8$ mm and $\varepsilon = 1.4$ mm.

III. Results and Discussion

A. Static Burst Pressure

Since the primary function of the diaphragm is to maintain the inflation pressure below the critical burst pressure before each shot, it is necessary to predict the burst pressure under a static load. Two key parameters of the diaphragm burst pressure are considered here, i.e., the diaphragm thickness and the groove depth. The burst pressure obtained from the experiments and simulations for different ε/t values at a diaphragm thickness of 1.8 mm is shown in Fig. 6. In the experiments, ε/t equals 0.722 and 0.778. Repeated tests were conducted for both. The simulation has the advantage of easier operation, and ε/t ranges from 0.5 to 0.9. For a given diaphragm thickness, a diaphragm with a higher ε/t value has a lower burst pressure. The burst pressure does not vary linearly with the depth, as observed in previous research, but exhibits an exponential trend. Bernier [11] proposed Eq. (4) to provide a rapid estimate of the burst pressure:

$$p = R\frac{t^{1.5}}{(\varepsilon/t)^{0.5} + 3.75(\varepsilon/t)^{3.5}} \tag{4}$$

However, this equation contains an open variable, R, which requires additional experiments to determine its value. In this study, the simulated burst pressure results were utilized to obtain suitable values for R, as depicted in Fig. 6. Despite selecting two R values with different ranges, a significant discrepancy between the experimental and simulation results remains, especially at $\varepsilon/t = 0.9$, approximately 30%.

Similar to Bernier's work, a new fitting correlation based on the calculation results can be obtained as

$$p = ct^a e^{b\varepsilon/t} \tag{5}$$

where a, b, and c are constants obtained from the Levenberg–Marquardt algorithm, a nonlinear surface fitting method. The expression of the diaphragm burst pressure for a given radius and groove width under the static load is obtained:

$$p = 47.74t^{1.295}e^{-4.768\varepsilon/t} \tag{6}$$

The estimated burst pressure obtained from this equation is shown in Fig. 6, resulting in an acceptable agreement between the simulated and experimental results. Unlike Eq. (4), Eq. (6) has no open variables. More simulations and experiments were conducted to validate the effectiveness of Eq. (6). In the simulations, t was 1, 2, 3, and 5 mm, and ε/t ranged from 0.5 to 0.9. In the experiments, t was 1 and 1.8 mm, and ε/t ranged from 0.7 to 0.9. The results are shown in Fig. 7, where the data on the abscissa are in the form of $t^{1.295}e^{-4.768\varepsilon/t}$.

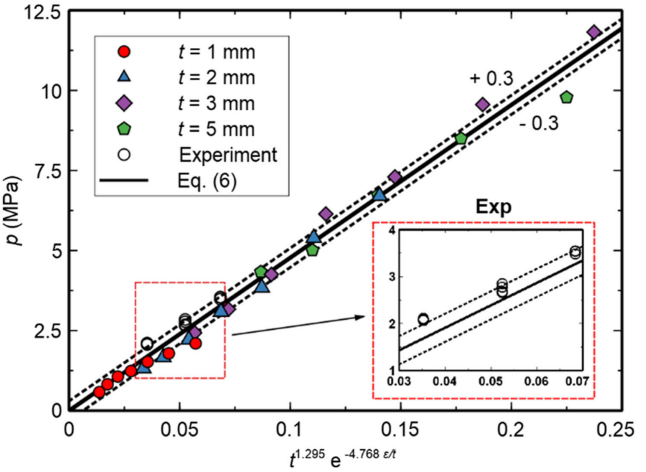

Fig. 7 Effect of diaphragm thickness and groove depth on burst pressure under a static load.

The simulated burst pressure agrees well with the experimental results. Our proposed correlation also shows good agreement for most cases, with a deviation within 0.3 MPa. Therefore, Eq. (6) is verified within the scope of this research.

In the above results, a constant groove width of 3.5 mm was maintained, corresponding to the groove width used in the experimental diaphragm. However, this study also conducted calculations with varying groove widths. The groove width is typically larger than 3 mm due to the practical challenges and costs associated with processing diaphragm groove widths below 3 mm. Consequently, our calculations considered diaphragm groove widths of 3.5, 5, and 7 mm; the results are illustrated in Fig. 8. A slight increase in the burst pressure is observed as the groove width increases. Nevertheless, the influence of the groove width on the burst pressure is relatively minor compared to the t and ε/t variables. Hence, the impact of the groove width is not extensively investigated, and a consistent groove width of 3.5 mm is maintained in subsequent analyses.

Numerical simulation methods offer a reliable and safe means of determining the burst pressure for existing test facilities and diaphragm structures, replacing physical experiments. Additionally, a new fitting formula was developed after extensive calculations to estimate the burst pressure rapidly. Note that the above results were obtained for conditions of 1 MPa $\le p \le$ 10 MPa, 1 mm $\le t \le$ 5 mm, and $0.5 \le \varepsilon/t \le 0.9$, covering the typical range.

B. Dynamic Burst Pressure

The previous section describes the diaphragm burst pressure under static loads. However, the rupture process of a diaphragm typically

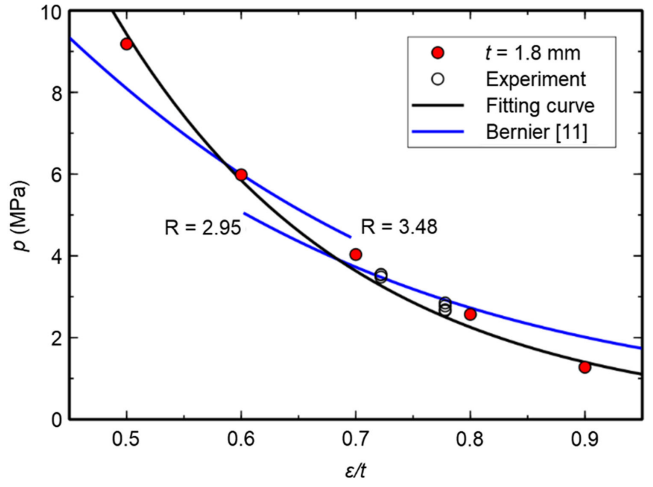

Fig. 6 Verification of simulation by experiments using an exponential fit and comparison with the existing equation.

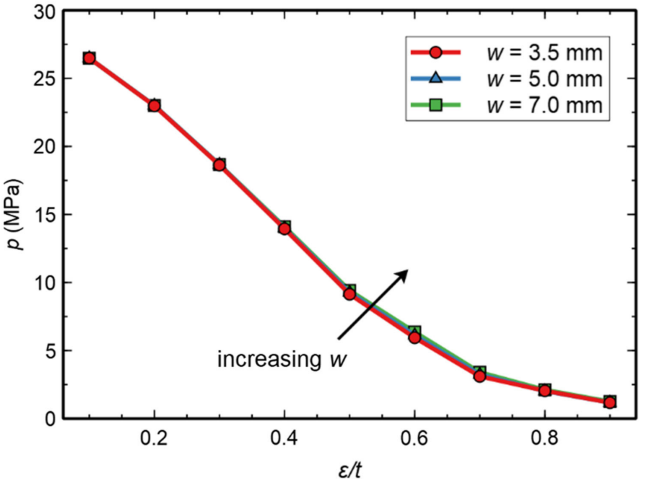

Fig. 8 Simulated burst pressure vs ε/t for different groove widths with $t = 1.8$ mm.

occurs under dynamic loads, as shown in Fig. 3 for three typical working conditions. This study first considers a case where the pressure increases instantaneously to a very high value with an extremely short duration for the pressure rise. The detonation case in Fig. 3 is such a case where the pressure rises to its peak quickly once the flammable gas mixture is ignited. The piezoelectric sensor in our experiments records data in the order of microseconds [27]. An impulse step load lasting 0.2 ms is adopted to represent this case. The load profiles are shown in the central insert in Fig. 9. In this paper, the "step load" is used to represent this load profile. This extreme comparison allows us to visualize the strain rate effect of the material exposed to burst pressure.

The burst pressure under step and static loads is shown in Fig. 9, where t is 1.0, 2.0, 3.0, and 5 mm, and ε/t ranges from 0.6 to 0.9. Figure 9 shows that the step load results in a higher burst pressure than the static load in all cases. The authors of Ref. [31] provide a stress–strain curve for stainless steel 304; the strengthening effect becomes more significant as the strain rate (1–1000 s^{-1}) increases. In addition, unlike static conditions, a dynamic load not only provides the strain energy for deformation but also generates the kinetic energy for high-speed motion. Due to the above reasons, a higher burst pressure exists under a step load. The damage and failure patterns of the structure under a dynamic load are closely related to the diaphragm thickness, the loading method, and the material properties. However, most structures of the diaphragms used in our lab fall within the range shown in Fig. 9.

In more common cases, the pressure increases to the burst pressure of a diaphragm at a certain time, as shown in the pressure profiles in Fig. 3 for the free-piston and combustion cases. In gas guns, the durations last in the order of 10 μs. Here, three sets of approximate dynamic load profiles are adopted to investigate the critical burst pressure of the diaphragms. The first one has a constant growth rate, i.e., a linear relationship between pressure and time, whereas the other two have variable rates extracted from two typical driving modes: combustion and free-piston modes (Fig. 3). The curves for the two cases derived from the experiments are fitted by simple functions:

$$p = \alpha\tau^3 \text{ for the combustion driving mode} \tag{7}$$

$$p = (\alpha - \beta\tau)^{-\gamma} \text{ for the free} - \text{piston driving mode} \tag{8}$$

where α, β, and γ are constants. The peak pressures of the variable-rate loads are higher than those of the constant rate load to ensure diaphragm rupture. The equations for the three dynamic profiles are

$$p = 5\tau/\tau_0 \tag{9}$$

$$p = 8(\tau/\tau_0)^3 \tag{10}$$

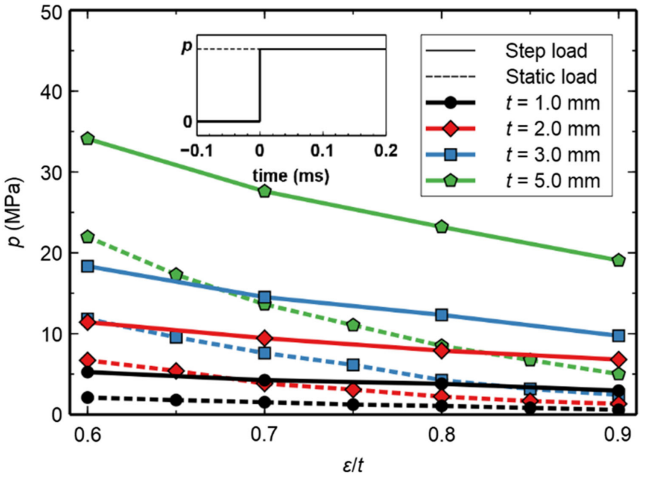

Fig. 9 Burst pressures under static and step loads.

$$p = 10/(5 - 4\tau/\tau_0)^3 \tag{11}$$

where τ is the current loading time, and τ_0 is the total time. In theory, the longer the loading time, the closer the results are to the static case. The burst pressures under dynamic loads at different times and under a static load were compared to understand this phenomenon (Fig. 10). The same diaphragm ($t = 2$ mm, $\varepsilon/t = 0.8$) was used with five loading durations (2, 5, 10, 20, and 40 ms) to change the average strain rate during the deformation. The dynamic loads were applied at

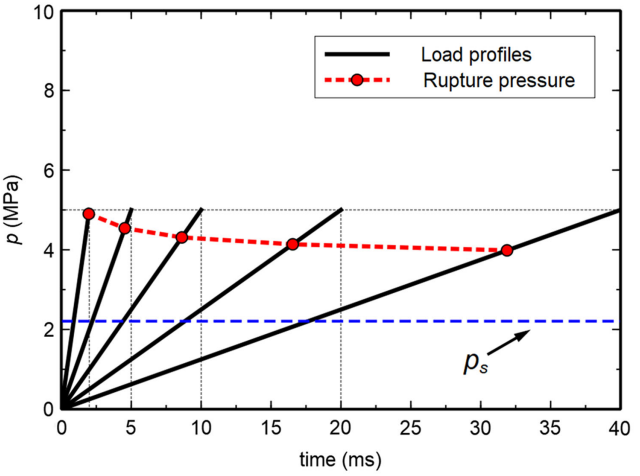

a) Result for loads with a constant growth rate with $p = 5\tau/\tau_0$

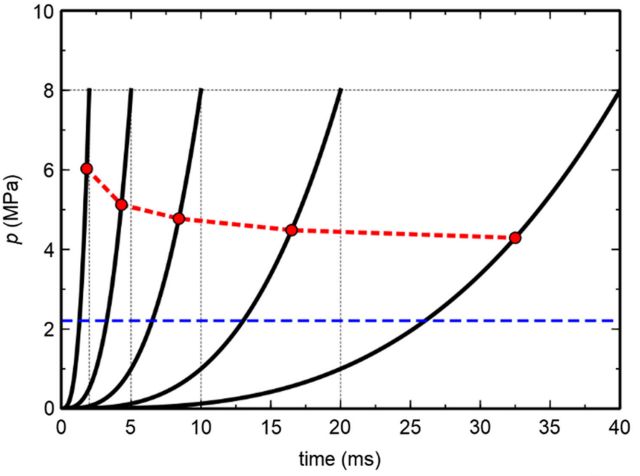

b) Result for loads with a variable growth rate with $p = 8(\tau/\tau_0)^3$

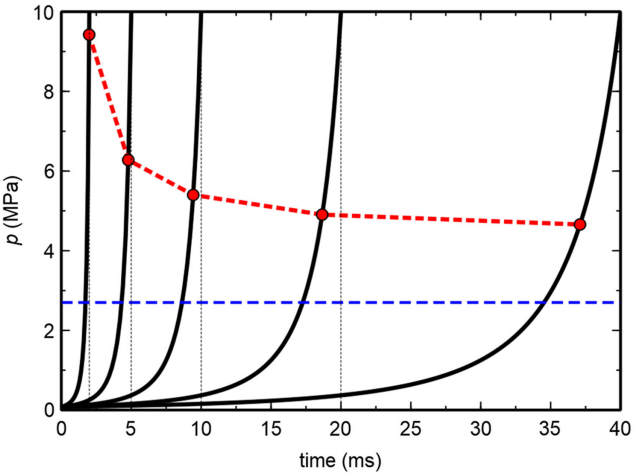

c) Result for loads with a variable growth rate with $p = 10/(5 - 4\tau/\tau_0)^3$

Fig. 10 Burst pressures of the diaphragm ($t = 2$ mm, $\varepsilon/t = 0.8$) under dynamic loads.

$\tau = 0$ s. The blue lines are the burst pressure under the static load for a specific diaphragm.

The results depicted in Fig. 10 reveal a consistent trend: as the duration increases, the burst pressure decreases and eventually levels off for all three loading cases. Notably, the burst pressures are higher for the three dynamic loads than for the static case. This disparity can be attributed to the relatively lower input momentum of the dynamic loads. Moreover, the diaphragm's burst pressure differs for the three load profiles. The material's strength diminishes as the loading duration increases due to the decreasing strain rate, whereas the failure strain remains relatively constant [31]. Consequently, a significant reduction in the threshold value of the rupture occurs as the loading rate decreases. This effect is particularly pronounced when the loading time is relatively short. Also, due to the accumulation of the strain rate strengthening effect, the faster increments of the rate of dynamic loads within the same loading durations increase the rupture pressures obviously, as shown in Figs. 10b and 10c. In general, the critical burst pressure of the diaphragm is between the pressure observed under static and dynamic loads, and its magnitude depends on the loading type, the loading rate, and the magnitude of the applied forces. Therefore, achieving an optimal diaphragm design necessitates the careful consideration and integration of these factors.

Note that the actual loading may differ from the above calculations since the pressure is closely related to the three-dimensional structure of the impulse facilities and the test conditions. Thus, the primary aim of the dynamic load analysis is to assess qualitatively the burst pressure disparity between dynamic and static loading profiles. However, the proposed burst pressure calculation method remains applicable if the type of pressure load is known.

IV. Conclusions

A numerical model was established to predict the burst pressure of flat-scored metal diaphragms in a shock tube. The influence of the diaphragm structures on the burst pressure was investigated, and an improved equation to estimate the static burst pressure rapidly was proposed. A good agreement was obtained between the simulation and experimental results. The proposed equation has better applicability and feasibility than the existing equation with an undetermined coefficient. Although the equation is based on a specific shock tube (JFX) and diaphragm material (stainless steel 304), the established process can be easily transplanted into other impulse facilities. The results of two types of time-varying loads (step and dynamic loads) on the diaphragm burst pressure were discussed. The burst pressure was higher under dynamic loads for the same diaphragm thickness and groove depth due to the strengthening effect of the material. As the loading time increased, the burst pressure was higher under a dynamic load than under a static load. The driving modes and operating conditions of shock tubes or shock tunnels significantly affect the burst pressure and diaphragm design.

Acknowledgments

This work was supported by the Key-Area Research and Development Program of Guangdong Province (Grant No. 2021B0909060004), the National Natural Science Foundation of China (Grant Nos. 12072352 and 12232018), and the Youth Innovation Promotion Association CAS (Grant No. 2021020).

References

[1] Tajima, K., Outa, E., and Nakada, G., "Some Investigations of Shock Tube Flow: On the Propagation Behavior of the Initial Shock Front," *Bulletin of JSME*, Vol. 11, No. 43, 1968, pp. 116–124. https://doi.org/10.1299/jsme1958.11.116

[2] Ikui, T., and Matsuo, K., "Investigations of the Aerodynamic Characteristics of the Shock Tubes (Part 1, The Effects of Tube Diameter on the Tube Performance)," *Bulletin of JSME*, Vol. 12, No. 52, 1969, pp. 774–782. https://doi.org/10.1299/jsme1958.12.774

[3] Brun, R., and Reboh, R., "Initial Flow Model in Shock Tubes," *AIAA Journal*, Vol. 15, No. 9, 1977, pp. 1344–1345. https://doi.org/10.2514/3.7423

[4] Gaetani, P., Guardone, A., and Persico, G., "Shock Tube Flows Past Partially Opened Diaphragms," *Journal of Fluid Mechanics*, Vol. 602, May 2008, pp. 267–286. https://doi.org/10.1017/S0022112008000815

[5] Satchell, M., Collen, P., McGilvray, M., and Di Mare, L., "Numerical Simulation of Shock Tube Flows Using Shock Tracking in an Overset Formulation," *AIAA Aviation 2020 Forum*, AIAA Paper 2020-2722, 2020. https://doi.org/10.2514/6.2020-2722

[6] Andreotti, R., Colombo, M., Guardone, A., Martinelli, P., Riganti, G., and di Prisco, M., "Performance of a Shock Tube Facility for Impact Response of Structures," *International Journal of Non-Linear Mechanics*, Vol. 72, June 2015, pp. 53–66. https://doi.org/10.1016/j.ijnonlinmec.2015.02.010

[7] Arun, K. R., Kim, H. D., and Setoguchi, T., "Effect of Finite Diaphragm Rupture Process on Microshock Tube Flows," *Journal of Fluids Engineering*, Vol. 135, No. 8, 2013, Paper 081203. https://doi.org/10.1115/1.4024196

[8] Mizuno, H., Sawada, K., and Sasoh, A., "Numerical Study of Non-Ideal Diaphragm Rupture in Expansion Tube," *40th AIAA Aerospace Sciences Meeting & Exhibit*, AIAA Paper 2002-0650, 2002. https://doi.org/10.2514/6.2002-650

[9] Pakdaman, S. A., Garcia, M., Teh, E., Lincoln, D., Trivedi, M., Alves, M., and Johansen, C., "Diaphragm Opening Effects on Shock Wave Formation and Acceleration in a Rectangular Cross Section Channel," *Shock Waves*, Vol. 26, No. 6, 2016, pp. 799–813. https://doi.org/10.1007/s00193-016-0628-1

[10] Vasil'ev, E. I., and Danil'chuk, E. V., "Numerical Solution of the Problem of Shock Tube Flow Development with Transverse Diaphragm Withdrawal," *Fluid Dynamics*, Vol. 29, No. 2, 1994, pp. 270–276. https://doi.org/10.1007/BF02324319

[11] Bernier, H., "Scaling and Designing Large-Bore Two-Stage High Velocity Guns," *High-Pressure Shock Compression of Solids VIII: The Science and Technology of High-Velocity Impact*, Springer, Berlin, 2005, pp. 37–83. https://doi.org/10.1007/3-540-27168-6_2

[12] Tang, W., Wang, Q., Wei, B., Li, J., Li, J., Shang, J., Zhang, K., and Zhao, W., "Performance and Modeling of a Two-Stage Light Gas Gun Driven by Gaseous Detonation," *Applied Sciences*, Vol. 10, No. 12, 2020, p. 4383. https://doi.org/10.3390/app10124383

[13] Mizoguchi, M., and Aso, S., "Numerical Study on Diaphragm Rupture for Performance Improvement of a Free Piston Shock Tunnel," *14th AIAA/AHI Space Planes and Hypersonic Systems and Technologies Conference*, AIAA Paper 2006-8110, 2006. https://doi.org/10.2514/6.2006-8110

[14] Tretjakovas, J., Kačianauskas, R., and Šimkevičius, Č., "FE Simulation of Rupture of Diaphragm with Initiated Defect," *Mechanics*, Vol. 62, No. 6, 2006, pp. 5–10.

[15] Colombo, M., Martinelli, P., and di Prisco, M., "Validation of a Computational Approach to Predict Bursting Pressure of Scored Steel Plates," *Experimental Mechanics*, Vol. 54, No. 9, 2014, pp. 1555–1573. https://doi.org/10.1007/s11340-014-9916-9

[16] Lyle, J. L., Guna, K. R., Kumar, P., and Sundararaj, A. J., "Rupture Dynamics of Shock-Tube Diaphragm," *2017 First International Conference on Recent Advances in Aerospace Engineering (ICRAAE)*, Inst. of Electrical and Electronics Engineers, New York, 2017, pp. 1–4. https://doi.org/10.1109/ICRAAE.2017.8297207

[17] Yuan, C. K., and Jiang, Z. L., "Experimental Investigation of Hypersonic Flight-Duplicated Shock Tunnel Characteristics," *Acta Mechanica Sinica*, Vol. 37, No. 3, 2021, pp. 422–433. https://doi.org/10.1007/s10409-020-01036-0

[18] Rast, J. J., *The Design of Flat-Scored High-Pressure Diaphragms for Use in Shock Tunnels and Gas Guns*, NAVORD Rept. 6865 (Ballistic Reprt. 29), U.S. Naval Ordance Lab., White Oak, MD, Sept. 1961.

[19] Helminiak, N. S., "Construction and Characterization of a Single Stage Dual Diaphragm Gas Gun," Doctoral Dissertation, Marquette Univ., Milwaukee, WI, 2017, p. 30.

[20] Prickett, P. W., "The Performance of Bursting Disks at Varying Rates of Pressurization," *The Protection of Exothermic Reactors and Pressurized Storage Vessels*, IChemE Symposium Series No. 85, U.K., 1984, pp. 83–90.

[21] Brill, A., Me-Bar, Y., Siman, M., Sadot, O., and Ben-Dor, G., "Diaphragm Gauge for Measuring Explosive Impulse," *International Journal of Impact Engineering*, Vol. 38, No. 8, 2011, pp. 765–769. https://doi.org/10.1016/j.ijimpeng.2011.04.003

[22] Jahnke, D., Azadeh-Ranjbar, V., Yildiz, S., and Andreopoulos, Y., "Energy Exchange in Coupled Interactions Between a Shock Wave and Metallic Plates," *International Journal of Impact Engineering*,

Vol. 106, Aug. 2017, pp. 86–102.
https://doi.org/10.1016/j.ijimpeng.2017.02.011
[23] Zhao, W., Jiang, Z. L., Saito, T., Lin, J. M., Yu, H. R., and Takayama, K., "Performance of a Detonation Driven Dhock Tunnel," *Shock Waves*, Vol. 14, No. 1, 2005, pp. 53–59.
https://doi.org/10.1007/s00193-004-0238-1
[24] Sasoh, A., Maemura, J., Hirakata, S., Takayama, K., and Falcovitz, J., "Diaphragm Rupture. Impingement by a Conically-Nosed, Ram-Accelerator Projectile," *Shock Waves*, Vol. 9, No. 1, 1999, pp. 19–30.
https://doi.org/10.1007/s001930050135
[25] Adair, D., Mukhambetiyar, A., Jaeger, M., and Malin, M., "The Influence of Finite Rupture Times on Flow Dynamics Within Micro-Shock Tubes," *International Journal of Computational Methods and Experimental Measurements*, Vol. 7, No. 2, 2019, pp. 106–117.
https://doi.org/10.2495/CMEM-V7-N2-106-117
[26] Rothkopf, E. M., and Low, W., "Diaphragm Opening Process in Shock Tubes," *Physics of Fluids*, Vol. 17, No. 6, 1974, pp. 1169–1173.
https://doi.org/10.1063/1.1694860
[27] Pakdaman, S. A., "Shock Wave Acceleration in a High-Aspect-Ratio Shock Tube," *Mechanical and Manufacturing Engineering*, Vol. 2014, Univ. of Calgary, Calgary, Canada, 2014, pp. 9–26.
https://doi.org/10.11575/PRISM/27777
[28] Kaneko, W., and Ishii, K., "Effects of Diaphragm Dupturing Donditions on Delf-Ignition of High-Pressure Dydrogen," *International Journal of Hydrogen Energy*, Vol. 41, No. 25, 2016, pp. 10,969–10,975.
https://doi.org/10.1016/j.ijhydene.2016.04.211
[29] Wang, Q., Luo, K., Li, J., Li, J., and Zhao, W., "Investigation of Dual Ignition for a Detonation-Driven Shock Tunnel in Forward Driving Mode," *Chinese Journal of Aeronautics*, Vol. 33, No. 5, 2020, pp. 1468–1475.
https://doi.org/10.1016/j.cja.2020.01.013
[30] Chen, H., Zhang, X. Y., and Yu, H. R., "Direct Initiation of Detonation with Ignition Tube," *Shock Waves*, Springer, Berlin, 2005, pp. 871–876.
https://doi.org/10.1007/978-3-540-27009-6_132
[31] Lu, X., Li, J., Zhang, X., Zhang, S., Wang, S., Chen, H., and Dong, Z., "Investigation of Combustion Driving Technology by Axial Synchronized Ignition for a Shock Tunnel," *LHD 2023 Summer Symposium*, Inst. of Mechanics, Hebei, China, 2023, pp. 1–14.
[32] Lin, Y. C., and Chen, X.-M., "A Critical Review of Experimental Results and Constitutive Descriptions for Metals and Alloys in Hot Working," *Materials & Design*, Vol. 32, No. 4, 2011, pp. 1733–1759.
https://doi.org/10.1016/j.matdes.2010.11.048
[33] Johnson, G. R., and Cook, W. H., "Fracture Characteristics of Three Metals Subjected to Various Strains, Strain Rates, Temperatures and Pressures," *Engineering Fracture Mechanics*, Vol. 21, No. 1, 1985, pp. 31–48.
https://doi.org/10.1016/0013-7944(85)90052-9
[34] Frontán, J., Zhang, Y., Dao, M., Lu, J., Gálvez, F., and Jérusalem, A., "Ballistic Performance of Nanocrystalline and Nanotwinned Ultrafine Crystal Steel," *Acta Materialia*, Vol. 60, No. 3, 2012, pp. 1353–1367.
https://doi.org/10.1016/j.actamat.2011.11.029
[35] Seo, J.-M., Jeong, S.-S., Kim, Y.-J., Kim, J.-W., Oh, C.-Y., Tokunaga, H., Kumagai, T., and Miura, N., "Modification of the Johnson–Cook Model for the Strain Rate Effect on Tensile Properties of 304/316 Austenitic Stainless Steels," *Journal of Pressure Vessel Technology*, Vol. 144, No. 1, 2021, Paper 011501.
https://doi.org/10.1115/1.4050833
[36] Meyers, M. A., *Dynamic Behavior of Materials*, Wiley, Hoboken, NJ, 1994, pp. 448–467.
https://doi.org/10.1002/9780470172278
[37] Taylor, G. I., and Quinney, H., "The Latent Energy Remaining in a Metal After Cold Working," *Proceedings of the Royal Society of London. Series A, Containing Papers of a Mathematical and Physical Character*, Vol. 143, No. 849, 1934, pp. 307–326.
https://doi.org/10.1098/rspa.1934.0004

C. Lee
Associate Editor